Change of lattice distortion images in X-ray topography with resonant scattering in the Laue case

Riichirou Negishi,[a]* Masami Yoshizawa,[a] Shengming Zhou,[a] Isao Matsumoto,[b] Tomoe Fukamachi[a] and Takaaki Kawamura[c]

[a]Saitama Institute of Technology, 1690 Fusaiji, Okabe, Ohsato, Saitama 369-0293, Japan, [b]Institute of Materials Structure Science, 1-1 Ouho, Tsukuba, Ibaraki 305-0801, Japan, and [c]University of Yamanashi, 4-4-37 Takeda, Kofu, Yamanashi 400-8510, Japan. E-mail: negishi@sit.ac.jp

Plane-wave topographs of X-rays for the GaAs 200 reflection were recorded using synchrotron radiation near the *K*-absorption edges of Ga and As. The topographic contrasts caused by lattice defects were changed by tuning the X-ray energy to four typical resonant scattering conditions. A sharp image of a lattice defect was observed when the Borrmann effect disappeared. When the Borrmann effect was conspicuous, an image of lattice distortion around a dislocation was observed, and its contrast was reversed by changing the phase factor of the resonant scattering. The lattice distortion image and its contrast reversal are discussed based on the resonant scattering dynamical theory by introducing the edge-dislocation model. The results show that topographs using resonant scattering should be a new characteristic method in synchrotron topography.

Keywords: X-ray topography; resonant scattering; GaAs; dislocation contrast; lattice distortion.

1. Introduction

The contrast of X-ray topographs of a crystal is formed as a result of the electric wavefield caused by dynamical diffraction being disturbed by distorted lattices in the crystal. The mechanism of contrast formation is explained on the basis of the X-ray dynamical theory of diffraction. The observation of topographic contrasts is useful in assessing the quality of a crystal, as some of the physical properties of the crystal depend on lattice defects resulting from dislocations in the crystal. For example, the threshold voltage of a field-effect transistor depends on the condition of dislocations (Miyazawa & Hyuga, 1986).

A conventional topograph is recorded using characteristic X-rays in the energy region in which atomic resonant scattering is negligibly small. Such topography gives clear images of lattice defects, hence it has been employed to examine the perfection of a crystal and the behavior of dislocations according to the contrast of the orientation and the extinction. Conspicuous progress has been made in assessment of crystal structure (Authier & Tanner, 1996; Bowen & Tanner, 1998). It is known that the Borrmann effect occurs even in a thick absorbing crystal, which has been utilized in the observation of microdefects. However, the conditions resulting in the Borrmann effect are not yet completely understood theoretically. The utilization is confined to qualitative analysis (Authier, 2001).

Recently, experiments have been performed under nuclear or atomic resonant scattering conditions in the advent of synchrotron radiation (Materlik *et al.*, 1994; Fukamachi *et al.*, 1993). Kato (1992) and Fukamachi & Kawamura (1993) presented independently a generalized dynamical diffraction formula which is valid even when the diffraction is induced only by resonant scattering (hereafter, such a theory is referred to as the *resonant scattering dynamical theory*). Theoretical studies on the features of dynamical diffraction with resonant scattering have been progressing, and several predicted effects have been confirmed by synchrotron radiation experiments (Fukamachi *et al.*, 1995, 1996; Negishi, Fukamachi, Yoshizawa *et al.*, 1998; Negishi, Fukamachi, Xu *et al.*, 1998). Topographs have been recorded using synchrotron radiation (*e.g.* Zontone *et al.*, 1996), but resonant scattering has not been fully utilized in it.

In this paper we report on the contrast changes of lattice defects in X-ray plane-wave topographs, which were recorded for the GaAs 200 reflection under different conditions of atomic resonant scattering by tuning the X-ray energy near the *K*-absorption edges of Ga and As (Negishi *et al.*, 2001). We discuss the contrast changes based on resonant scattering dynamical theory by introducing the lattice distortion model around the defects. We use the GaAs 200 reflection, as the structure factor without resonant scattering is very small and the effect of resonant scattering should be exhibited more strongly than that of Thomson scattering.

2. Theoretical consideration

2.1. Resonant scattering dynamical theory

According to the resonant scattering dynamical theory, the basic equation in the two-beam approximation is given for the **h** reflection as

$$\left[\left(\mathbf{k}_0^2\right)^{1/2} - \kappa_0\right]\left[\left(\mathbf{k}_h^2\right)^{1/2} - \kappa_0\right] = \frac{P^2\kappa_{0r}^2}{4}\,\chi_h\chi_{-h}. \tag{1}$$

Here, $\mathbf{k}_0$ and $\mathbf{k}_h$ are wavevectors of the incident and diffracted beams, respectively, and P is the polarization factor. The mean wavenumber in crystal κ_0 is complex and is given by $\kappa_0 = \kappa_{0r} + i\kappa_{0i}$, with its real part $\kappa_{0r} = K(1 + \chi_{0r}/2)$ and its imaginary part $\kappa_{0i} = K\chi_{0i}/2$, K being the wavenumber in a vacuum. Atomic units ($\hbar = m = e = 1$) are used. χ_{hr} and χ_{hi}, which are Fourier coefficients of the real and imaginary parts of the X-ray polarizability $\chi(\mathbf{r})$, respectively, are defined as

$$\chi_{hr} = -\frac{4\pi}{V\omega^2}\sum_j \left(f_j^0 + f_j'\right)\exp\left(i\,\mathbf{h}\cdot\mathbf{r}_j\right)T_j, \tag{2}$$

$$\chi_{hi} = -\frac{4\pi}{V\omega^2}\sum_j f_j''\exp(i\,\mathbf{h}\cdot\mathbf{r}_j)\,T_j. \tag{3}$$

Here, V is the unit-cell volume, ω is the X-ray energy, f_j^0 is the normal atomic scattering factor of the jth atom, f_j' and f_j'' are the real and the imaginary parts of anomalous scattering factor, respectively, **h** is the reciprocal lattice vector, $\mathbf{r}_j$ is the position vector and T_j is the temperature factor. The right-hand side of equation (1) can be rewritten as

$$\chi_h\chi_{-h} = \left(|\chi_{hr}|^2 + |\chi_{hi}|^2\right)(u + \mathrm{i}v), \tag{4}$$

where

$$u = \left(|\chi_{hr}|^2 - |\chi_{hi}|^2\right)/\left(|\chi_{hr}|^2 + |\chi_{hi}|^2\right), \tag{5}$$

$$v = \left(1 - u^2\right)^{1/2}\cos\delta. \tag{6}$$

The phase difference δ between χ_{hr} and χ_{hi} is defined as

$$\delta = \arg(\chi_{hr}) - \arg(\chi_{hi}). \tag{7}$$

The resonant scattering condition changes with the energy ω of the incident X-rays. The valid scope of $(u + \mathrm{i}v)$ in the complex plane is the region enclosed by the unit circle, where $-1 \le u \le 1$ (see Fig. 1). For a crystal with a center of symmetry, $|\chi_h| = |\chi_{-h}|$ holds and δ is

  DOI: 10.1107/S0909049504001992

either 0 or π, then (u, v) is located on the unit circle. Otherwise, $|\chi_h| \neq |\chi_{-h}|$, (u, v) is located at some point inside the unit circle because $\cos\delta$ is less than unity.

As shown in Fig. 1, at point A, $(u, v) = (1, 0)$ and $\chi_{hi} = 0$. The diffraction is induced only by χ_{hr} in this case. At point B, $(u, v) = (0, -1)$ and $|\chi_{hr}| = |\chi_{hi}|$, then $\delta = \pi$ and the sign of χ_{hr} is different from that of χ_{hi}. At point C, $(u, v) = (-1, 0)$ and $\chi_{hr} = 0$. Only χ_{hi} remains non-zero and the dynamical diffraction is induced only by resonant scattering. At point D, $(u, v) = (0, 1)$ and $|\chi_{hr}| = |\chi_{hi}|$, then $\delta = 0$ and the sign of χ_{hr} is the same as that of χ_{hi}.

2.2. Features of rocking curves at four typical resonant conditions

χ_{hr} and χ_{hi} for the GaAs 200 reflection are shown in Fig. 2, calculated near the K-absorption edges of Ga and As. In the calculation, the origin of the coordinate is chosen at a Ga site. The anomalous scattering factors are calculated by the method of Parratt & Hempstead (1954), in which the oscillation strength of g_k at an absorption edge given by Cromer (1965) is employed. Because $|\chi_h| = |\chi_{-h}|$ holds for the GaAs 200 reflection, the points A, B, C and D shown in Fig. 2 correspond to those shown in Fig. 1. Fig. 3 shows the diffracted (P_h) and transmitted (P_d) rocking curves in the Laue case, calculated by using the atomic scattering factors corresponding to the points A, B, C and D in Fig. 2, and by assuming a crystal thickness of 133 µm and a temperature factor $B = 0.64$ Å^2 for both Ga and As. Different shapes of rocking curves are demonstrated clearly under the diffraction conditions of A, B, C and D.

The condition $(u, v) = (1, 0)$ at point A can be satisfied even when absorption exists in a polyatomic crystal like GaAs, and the dynamical effect induced only by χ_{hr} is obtained. In this case the diffracted and transmitted rocking curves are symmetric with respect to the exact Bragg angle, and Pendellösung beat appears (see Fig. 3*a*). There is no anomalous transmission of the Borrmann effect under this condition, which can be understood by noting the following three aspects: (i) the transmitted rocking curve is symmetric; (ii) the intensity of the transmitted beam is always weaker than the intensity (dotted lines) given by the mean absorption coefficient (μ_0); (iii) as can be seen by the averaged line (broken line) of the rocking curves with the Pendellösung beat, there is a peak in the diffracted curve but a valley in the transmitted curve in the center. The vanishing of the Borrmann effect leads to the large width of the transmitted and diffracted rocking curves. This results in those topographic images which are not sensitive to the lattice distortions around defects. Then the defect image appears to be narrow in width.

When $(u, v) = (-1, 0)$ at point C, the dynamical effect induced only by χ_{hi} can be obtained, and the Borrmann effect appears regardless of the crystal thickness (Fukamachi & Kawamura, 1993). Fig. 3(*c*) shows the rocking curves in this case. The transmitted intensity becomes strong together with the diffracted intensity around the Bragg angle. The transmitted intensity is always stronger than that (dotted line) estimated by the mean absorption coefficient. This suggests that the Borrmann effect is reflected in the rocking curves. In addition, both the diffracted and transmitted rocking curves are symmetric.

Fig. 3(*b*) shows the rocking curves corresponding to point B with the condition $(u, v) = (0, -1)$, and Fig. 3(*d*) shows those corresponding to point D with the condition $(u, v) = (0, 1)$. The Borrmann effect emerges conspicuously both in Figs. 3(*b*) and 3(*d*) just like in Fig. 3(*c*). It must be noted here, however, that the transmitted rocking curves are asymmetric although the diffracted curves are symmetric with respect to the exact Bragg angle. As seen in the transmitted rocking curves, the tail of the peak is higher on the right-hand side than that on the left-hand side in Fig. 3(*b*). On the other hand, the tail is higher on the left-hand side in Fig. 3(*d*). The change of asymmetry originates from the sign change of v, *i.e.* the change of δ from π to 0.

3. Experiment

The sample of GaAs used in the experiment was manufactured by Sumitomo Electric Industries. It was doped with a very low concentration of Si of thickness 133 ± 1 µm and with an EPD (etch pit density) value of less than 500 cm^{-2}. The experiment was performed on beamline 15C at KEK-PF. The X-rays from synchrotron radiation were monochromated by a Si 111 double-crystal monochromator, and radiation with σ-polarization was used. XANES was measured by using a thin sheet of Ge to calibrate the monochromator according to the quantitative criterion of the Ge K-absorption edge (11306 ± 0.5 eV).

The measured rocking curves for GaAs 200 are shown in Fig. 4. The X-ray energies in Figs. 4(*a*), 4(*b*), 4(*c*) and 4(*d*) correspond to the

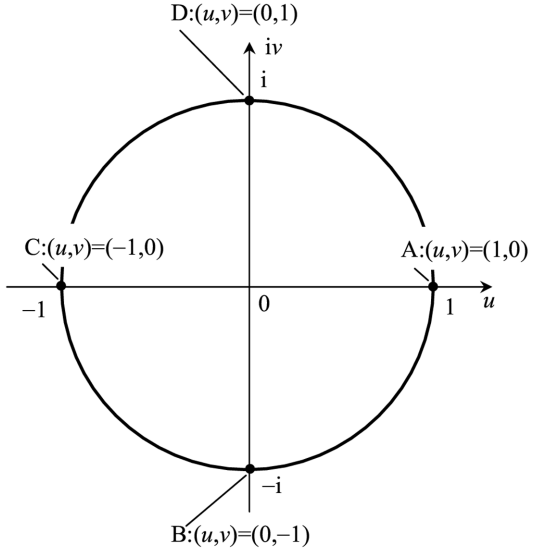

Figure 1
The unit circle in the complex plane (u, v). Values u and v are varied on and inside the unit circle. Four typical resonant conditions, A, B, C and D, are indicated.

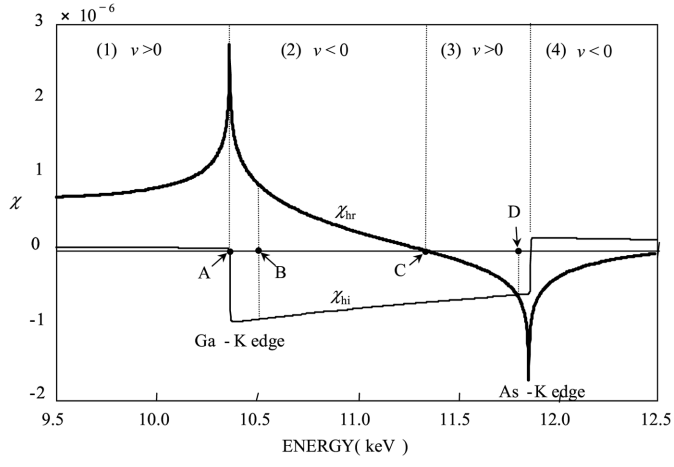

Figure 2
χ_{hr} and χ_{hi} for the GaAs 200 reflection. u and v change with the energy of the incident X-ray. Here, A, B, C and D correspond to the points in Fig. 1.

conditions at A, B, C and D, respectively, in Fig. 1. One can see typical features at the condition $(u, v) = (1, 0)$ in Fig. 4(a). The transmitted intensities (filled circles) decrease with the increase of the diffracted intensities (open circles), and the intensities in the higher- and lower-angle sides are almost equal as seen in the transmitted rocking curve. This clearly shows that the condition $(u, v) = (1, 0)$ holds. In the same way, it is determined that the condition $(u, v) = (-1, 0)$ holds in Fig. 4(c). The transmitted intensity increases with the increase of the diffracted intensity (the anomalous transmission of the Borrmann effect), and the intensities in the higher- and lower-angle sides are almost equal as seen in the transmitted rocking curves. The decrease of intensity with deviation from the peak at the high-angle side is slower than that at the low-angle side as seen in the transmitted rocking curve in Fig. 4(b). The same trend can be seen in the calculated curve in Fig. 3(b). It is confirmed that the condition corresponding to point B is satisfied. On the other hand, the reversed trend can be seen both in the observed (Fig. 4d) and calculated (Fig. 3d) rocking curves; the condition corresponding to point D is satisfied experimentally.

The diffracted- and transmitted-beam topographs were recorded using a nuclear plate (ILFORD L4, emulsion thickness 50 μm) placed 20 mm downstream of the sample at the intensity peak of the diffracted beam. The exposure time was changed between 0.5 and 30 s depending on the intensity.

4. Results and discussion

The obtained topographic images at the four diffraction conditions in Figs. 3(a), 3(b), 3(c) and 3(d) are shown in Figs. 5(a), 5(b), 5(c) and 5(d), respectively. The upper panel of each figure shows the transmitted-beam image, and the lower panel shows the diffracted-beam image. Darker contrast corresponds to the stronger X-ray intensity. In the images of Fig. 5, we focus on the linear defect images running from the upper left to the lower right. The scratch on the crystal surface was not seen in the optical photograph on either sides of the region corresponding to the image. The diffracted-beam topographs in Fig. 5(a) recorded under the condition corresponding to point A gives the sharpest image among those taken under the four conditions. The intensities from the defect become strong. This sharp contrast can be explained by the fact that the influence of the surrounding distortion of the dislocation becomes less as the width of the rocking curves increases, as expected from Fig. 3(a). In addition, the contrast of the transmitted-beam image is the reverse of that of the diffracted-beam image, which is consistent with the fact that the transmitted intensity becomes weak when the diffracted intensity becomes strong, as shown in Fig. 3(a).

The topographs recorded under the condition of point C are shown in Fig. 5(c). The topographic images were recorded when the Borrmann effect was enhanced most conspicuously. As seen in the transmitted- or diffracted-beam topographs shown in Fig. 5(c), the defect image running from the upper left to the lower right consists of two white linear parts. These are the regions with defects and their surrounding distortions, where the anomalous transmission of the Borrmann effect vanishes. The broadened white line implies that the Borrmann effect is sensitive to the distortions around the defects. By comparing the contrast of the diffracted-beam image with that of the transmitted-beam image, it can be seen that the white–black contrasts are reversed in Fig. 5(a) but the two linear parts are always white in Fig. 5(c). The contrast in Fig. 5(c) originates from the fact that the transmitted-beam

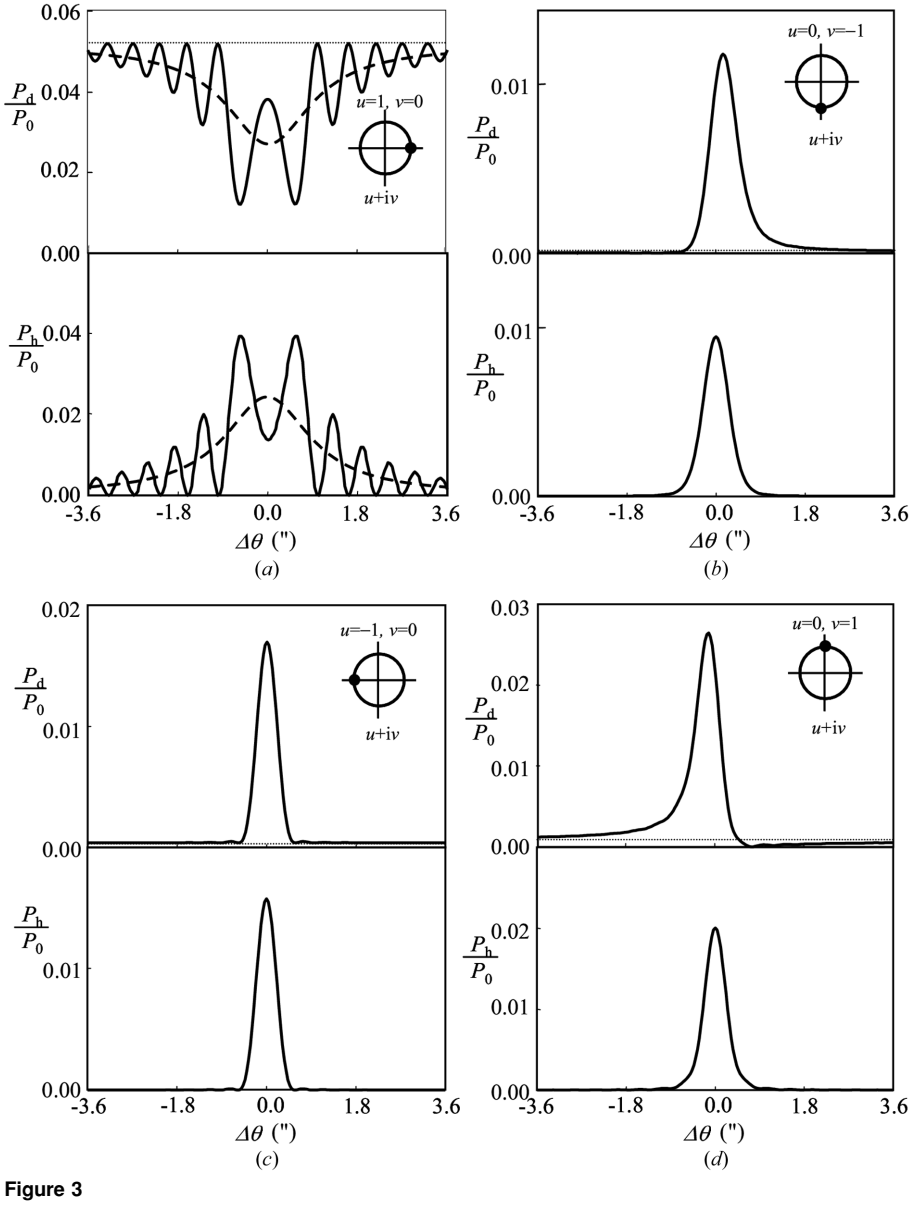

Figure 3
Calculated transmitted and diffracted rocking curves for the GaAs 200 reflection with a crystal thickness of 133 μm and the temperature factor $B = 0.64$ A^2 for (a) 10.3645 keV, (b) 10.5020 keV, (c) 11.3430 keV and (d) 11.8050 keV. (a), (b), (c) and (d) correspond to the resonant scattering conditions A, B, C and D, respectively, in Fig. 1. Dotted lines correspond to the intensities given by the mean absorption coefficient (μ_0) and broken lines correspond to the averaged values for the rocking curves with the Pendellösung beat. The inset circle denotes the diffraction condition in the (u, v) plane.

intensity increases together with the diffracted-beam intensity owing to anomalous transmission as shown in Fig. 3(*c*). The number of broadened white specks in Fig. 5(*c*) is larger than that in Fig. 5(*a*). This means that the distortions caused by small defects, which cannot be observed in Fig. 5(*a*), are observable in Fig. 5(*c*). This also shows that the topograph in Fig. 5(*c*) is more sensitive to the distortion than that in Fig. 5(*a*).

The linear defect images running from the upper left to the lower right in Figs. 5(*b*) and 5(*d*) appear white as the influence of the Borrmann effect becomes conspicuous, just the same as that shown in Fig. 5(*c*). The contrasts of the two broad lines in the transmitted-beam image (I_d) in Figs. 5(*b*) and 5(*d*) are different from each other; the lower white line is brighter than the upper white line in Fig. 5(*b*) but the contrasts are reversed in Fig. 5(*d*). The contrasts in the diffracted-beam image (I_h) are reverse of those in the transmitted-beam image in Figs. 5(*b*) and 5(*d*). Fig. 6 shows a cross section of the two lines of the transmitted-beam images in Figs. 5(*b*) and 5(*d*). The left-hand panels show the enlarged parts and the lines indicate those along which the cross-section contrasts are measured. The right-hand panels show the cross-section contrasts. *A*, *B* and *C* in the right-hand panels show the brightness variation along the corresponding lines in the left-hand topographs. The height shows the dark level. The two white lines correspond to two valleys. The height varies from position to position, but the left-hand valley is always lower than the right-hand valley in Fig. 6(*a*), and the left-hand valley is always higher in Fig. 6(*b*). The contrast difference originates from the asymmetry of the transmitted rocking curve as seen in Figs. 3(*b*) and 3(*d*). The contrast reversal of the two lines in the transmitted- and diffracted-beam images can be understood according to the conservation of the X-ray beam flux (Negishi *et al.*, 2001). In order to confirm that the contrasts in the transmitted-beam image do not originate in the setting error of the incident angle, the diffracted images were recorded under the same conditions as that of Fig. 5(*c*) but at the higher-angle side where the diffracted intensity is half of the maximum. The diffracted-beam images are shown in Fig. 7. The contrasts of the two white lines are almost the same. It is clear that the contrasts of the two white lines seen in Fig. 5(*b*) are not caused by the setting error. Similarly, the contrasts of the two white lines in Fig. 5(*d*) are reversed in comparison with those in Fig. 5(*b*). This can be understood by noting that the asymmetry of the transmitted rocking curve in Fig. 3(*d*) is reversed in comparison with Fig. 3(*b*).

In order to discuss the asymmetry of the two linear defects and their contrast reversal in Figs. 5(*b*) and 5(*d*), we introduce an edge-dislocation model as shown in Fig. 8 (Weertman & Weertman, 1992). We assume that an extra half plane **p** is parallel to the lattice plane for the diffraction, that both of these planes are normal to the crystal surface and the dislocation line *l* is parallel to the surface. In this case the dislocation contrast should be largest among others. We also assume that the distorted angles $|\Delta|$ of the diffraction lattice plane are symmetric for the left-hand and the right-hand side of the extra plane. When the Borrmann effect is conspicuous, the distortion contrast becomes white owing to the Borrmann effect vanishing if the distortion angle is more than the full width at half-maximum (FWHM) of the rocking curve. The distorted lattice planes are inclined to the lower-angle side in the left-hand side of the extra plane and to the higher-angle side in the right-hand side as shown in Fig. 8. As X-rays are diffracted by such distorted planes, two white lines appear in the transmitted-beam images. When the rocking curve is symmetric with respect to the exact Bragg angle, as in the case of *C*, the two white lines show the same contrast. In the case of *B*, however, the intensity of the tail in the higher-angle side is higher than that in the lower-angle side, the right-hand side of the two white lines is darker than the left-hand side. Similarly, in the case of *D*, the intensity of the tail in the higher-angle side is lower than that in the lower-angle side, the right-hand side of the white two lines is brighter than the left-hand side.

Next we discuss the validity of the above argument based on the dynamical theory. According to the rocking curve of the transmitted wave in Figs. 3(*b*) and 3(*d*), the asymmetry is discernible up to about five times the FWHM. As the FWHM of the rocking curve in Figs. 4(*b*) and 4(*d*) is about 7″, the topographic images of white contrast can be observed if the distortion angle is more than 3.5″. On the other hand, assuming that the displacement *R* is about the same as the lattice constant (Fig. 8), the angle $|\Delta|$ is estimated to be in the range of 1.7–5.1″ from the transmitted image in Fig. 5(*d*). Since this angle range is almost the same as the angle range of the asymmetry of the observed rocking curve (3.5″), it is justified that the contrast change in Fig. 6 and its reversal can be discussed based on the dynamical theory. For this reason it can be said that the phase information of χ_h should be reflected in the contrasts of defect images in Figs. 5(*b*) and 5(*d*). It is useful to investigate the Burgers vector of the dislocation in this case, which will be published elsewhere.

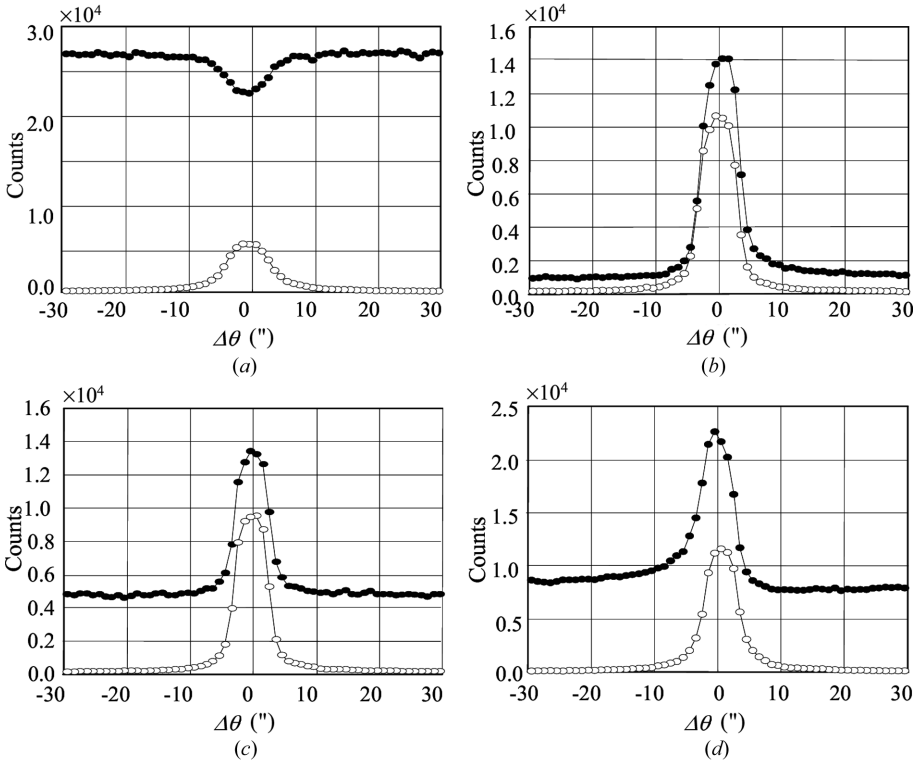

Figure 4
Measured rocking curves for the GaAs 200 reflection for (*a*) 10.362 keV, (*b*) 10.502 keV, (*c*) 11.343 keV and (*d*) 11.805 keV. (*a*), (*b*), (*c*) and (*d*) correspond to the same conditions as those in Fig. 3. Open circles: P_d. Filled circles: P_h.

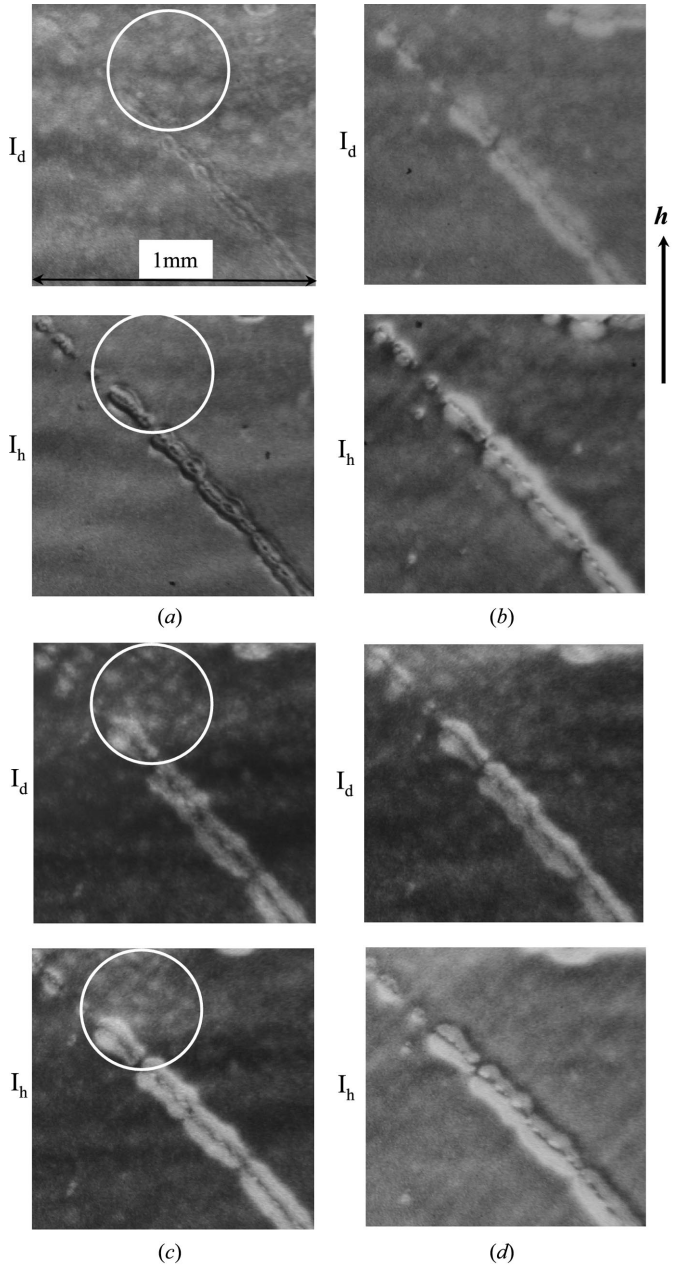

Figure 5
Recorded X-ray topographs for the transmitted beam (upper panel) and the diffracted beam (lower panel) at the peak intensity of the diffracted beam with energies (*a*) 10.362 keV, (*b*) 10.502 keV, (*c*) 11.343 keV and (*d*) 11.805 keV. **h** is the reciprocal lattice vector.

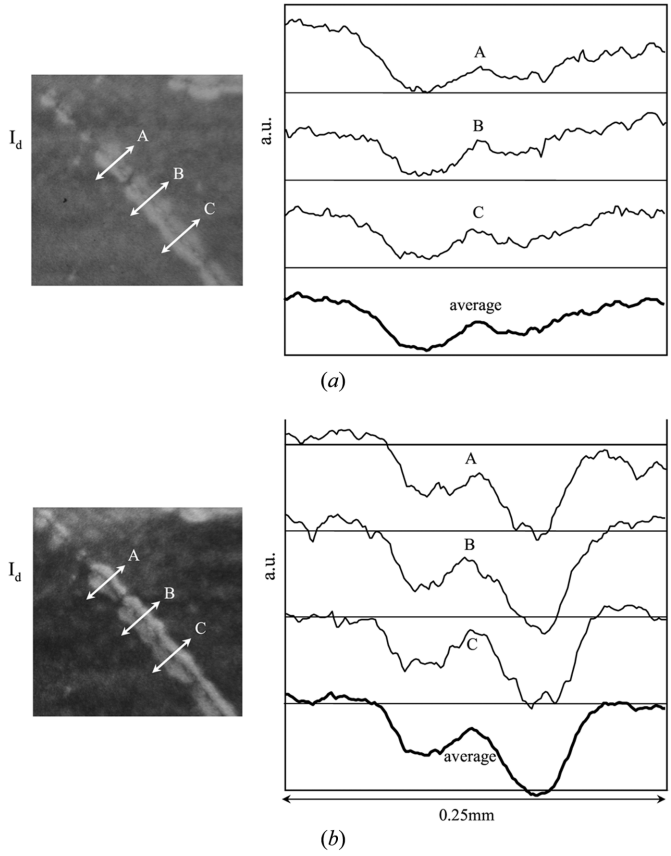

Figure 6
Cross-section contrasts for (*a*) 10.502 keV and (*b*) 11.805 keV. Each left-hand panel shows a part of the image in Figs. 5(*b*) and 5(*d*). Each right-hand panel shows the cross-section contrasts along the lines indicated in the left-hand panel. The height shows the dark level. The valley corresponds to the white image in the topographs.

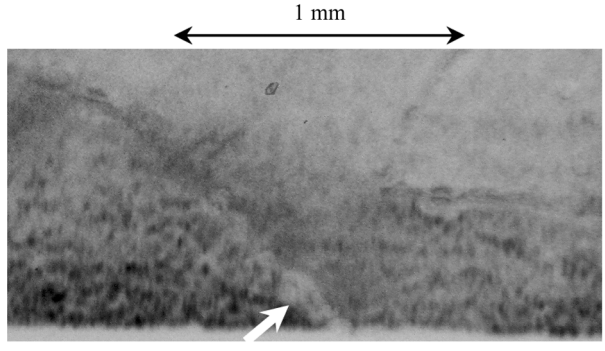

Figure 7
Diffracted-beam topograph recorded under the same condition as in Fig. 5(*c*) but at the higher-angle side where the diffracted intensity is half of the maximum.

5. Summary

Topographs were recorded under four typical resonant scattering conditions. The characteristic changes in the rocking curves predicted by theory were clearly observed. In the case of $(u, v) = (1, 0)$, the scattering is induced only by χ_{hr}, and the Borrmann effect vanishes completely even in an absorbing crystal. The region with defects becomes dark in the transmitted-beam topographs, and sharp defect images are obtained in the diffracted-beam topographs. This clearly shows an advantage of using resonant scattering. In the case of $(u, v) = (-1, 0)$, the scattering is induced only by χ_{hi}, and the Borrmann effect becomes very conspicuous even in a thin crystal. In the defect regions, the Borrmann effect vanishes and the regions are observed white and broadened. This suggests that the distribution of distortions caused by lattice defects are sensitively observed. For instance, the images of the lattice distortions caused by tiny defects, which are not observed under the condition of $(u, v) = (1, 0)$, can be observed in this case. In the case of $(u, v) = (0, \pm 1)$, the Borrmann effect is also conspicuous as in the case of $(u, v) = (-1, 0)$. In addition, the contrasts are different between $v = 1$ and $v = -1$, *i.e.* $\delta = 0$ and $\delta = \pi$. The contrast difference can be discussed based on the resonant scattering dynamical theory, by using the edge-dislocation model.

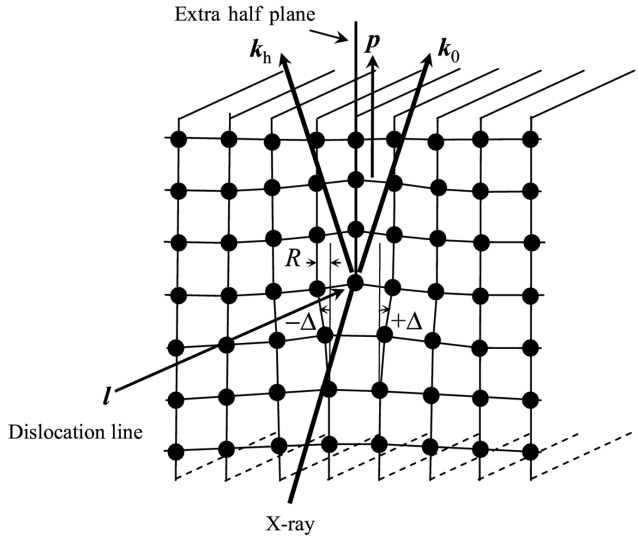

Figure 8
The edge-dislocation model. R and Δ express the displacement and the angle of the distortion due to a dislocation with an extra half plane **p**.

Topography using resonant scattering is expected to be useful in examining the perfection of a crystal and the details of the dislocation.

In the present experiment the divergence angle of the quasi-plane wave from the monochromator was about ten times larger than that from the sample crystal. Even with this large divergent angle of the incident X-rays the phase information was reflected in the lattice distortion images. By improving the divergence angle in the experiment, topographs with more conspicuous characteristics of the dynamical effect with resonant scattering can be recorded. In the present paper the topography in the Laue case is studied. It can be extended to the Bragg case, which has been published elsewhere (Fukamachi *et al.*, 2002).

The authors are particularly indebted to Professor Tokonami of Saitama Institute of Technology (SIT) for his valuable discussion, and are deeply grateful to Dr K. Hirano and Dr Zhang for help in experiments during this study. The experiment was carried out with the approval of the Photon Factory Program Advisory Committee, proposal No. 2000G046. This work was financially supported by the Advanced Science Research Laboratory of SIT. One of the authors (RN) was supported by a Grant-in-Aid (No. 12650018) for Scientific Research from the Ministry of Education, Culture, Sports, Science and Technology.

References

Authier, A. (2001). *Dynamical Theory of X-ray Diffraction.* Oxford University Press.
Authier, A. & Tanner, B. K. (1996). *X-ray and Neutron Dynamical Diffraction.* New York: Plenum Press.
Bowen, D. K. & Tanner, B. K. (1998). *High Resolution X-ray Diffractometry and Topography.* London: Taylor and Francis.
Cromer, D. T. (1965). *Acta Cryst.* **18**, 17–23.
Fukamachi, T. & Kawamura, T. (1993). *Acta Cryst.* A**49**, 384–388.
Fukamachi, T., Negishi, R. & Kawamura, T. (1995). *Acta Cryst.* A**51**, 253–258.
Fukamachi, T., Negishi, R., Yoshizawa, M., Ehara, K., Kawamura, T., Nakajima, T. & Zhao, Z. (1993). *Acta Cryst.* A**49**, 573–575.
Fukamachi, T., Negishi, R., Zhou, S., Yoshizawa, M. & Kawamura, T. (2002). *Acta Cryst.* A**58**, 552–558.
Fukamachi, T., Negishi, R., Zhou, S., Yoshizawa, M., Sakamaki, T., Kawamura, T. & Nakajima, T. (1996). *Acta Cryst.* A**52**, 669–674.
Kato, N. (1992). *Acta Cryst.* A**48**, 829–833.
Materlik, G., Sparks, C. J. & Fischer, K. (1994). Editors. *Resonant Anomalous X-ray Scattering.* Amsterdam: North-Holland.
Miyazawa, S. & Hyuga, F. (1986). *IEEE Trans. Electron Devices*, ED**33**, 227–233.
Negishi, R., Fukamachi, T., Xu, Z., Yoshizawa, M., Matsumoto, I., Kawamura, T. & Nakajima, T. (1998). *Jpn. J. Appl. Phys.* **37**, 4014–4015.
Negishi, R., Fukamachi, T., Yoshizawa, M., Zhou, S., Xu, Z., Matsumoto, I., Kawamura, T. & Nakajima, T. (1998). *J. Appl. Cryst.* **31**, 351–355.
Negishi, R., Yoshizawa, M., Zhou, S., Matsumoto, I., Fukamachi, T. & Kawamura, T. (2001). *Jpn. J. Appl. Phys.* **40**, L884–L887.
Parratt, L. G. & Hempstead, C. F. (1954). *Phys. Rev.* **94**, 1593–1600.
Weertman, J. & Weertman, J. R. (1992). *Elementary Dislocation Theory.* Oxford University Press.
Zontone, F., Mancini, L., Barrett, R., Baruchel, J., Hartwig, J. & Epelboin, Y. (1996). *J. Synchrotron Rad.* **3**, 173–184.

 Received 15 November 2003 • Accepted 27 January 2004